Downloaded via CARNEGIE MELLON UNIV on March 08, 2025 at 06:46:59 (UTC). See https://pubs.acs.org/sharingguidelines for options on how to legitimately share published articles.

ACS APPLIED NANO MATERIALS Cite This: ACS Appl. Nano Mater. 2019, 2, 3280−3291 Article www.acsanm.org

High Performance Flexible Temperature Sensors via Nanoparticle Printing

Md Taibur Rahman,[†,⊥] Chih-Yang Cheng,[†] Burcu Karagoz,[‡] Mike Renn,[∥] Matthew Schrandt,[∥] Andrew Gellman,[‡,§] and Rahul Panat*[,†,§]

[†]Department of Mechanical Engineering, [‡]Department of Chemical Engineering, and [§]W. E. Scott Institute for Energy Innovation, Carnegie Mellon University, Pittsburgh, Pennsylvania 15213, United States

[∥]Optomec Inc., St. Paul, Minnesota 55114, United States

Supporting Information

ABSTRACT: Deformable temperature sensors are required for applications such as soft robotics, biometric sensing, cryopreservation of organs, and flexible electronics. In this paper, we demonstrate Cu−CuNi temperature sensors on flexible Kapton substrates by a novel method consisting of rapid aerosol jet printing of nanoparticles followed by laser sintering at low powers of 100 mW and 400 mW under a shroud of an inert gas to minimize oxidation. The sensors showed a highly linear response as a function of the temperature and the highest sensitivity among film-based sensors yet reported in literature (Rajagopal, M. C.; et al. *Sens. Actuators, A* **2018**, *272*, 253; Yang, F.; et al. *Sci. Rep.* **2017**, *7* (1), 1721; Murakami, R.; et al.*J. Cryst. Growth* **2018**, *487*, 72−77). The sensor film microstructure was investigated using scanning electron microscopy (SEM), X-ray photoemission spectroscopy (XPS), transmission electron microscopy (TEM), and selective area electron diffraction (SAED). The Cu and CuNi film morphology consisted of fused nanoparticles with varying degrees of coalescence and porosities ranging from 9% to 24% through the thickness of the films. No surface oxidation was observed for CuNi films but oxide phase was detected for the Cu films, which did not affect the sensor performance after repeated tests up to a temperature of 140 °C. The sensor performance was independent of the manufacturing conditions of the aerosol jet printing process. Flexibility tests showed a stable device performance (variation of Seebeck coefficient within 2.5%) after 200 bending cycles at three different radii and 200 twisting cycles. The superior performance of the sensor films to the bending and twisting tests was attributed to the porosity of the sintered nanoparticles that allows significant strain without a proportional build-up of the stresses in the film. These results demonstrate the suitability of nanoparticle-based bottom-up fabrication methods for a range of deformable high-performance electronic devices.

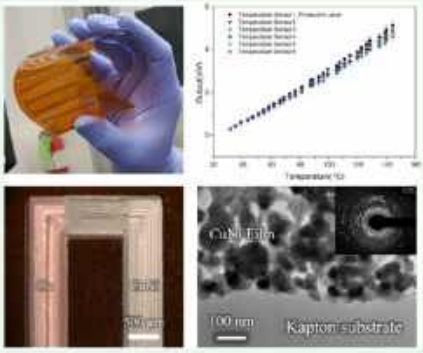

KEYWORDS: *printed electronics, nanoparticles, thermocouple, flexible sensors, aerosol jet printing, 3D printing, additive manufacturing, printed thin films*

1. INTRODUCTION

Conformal flexible sensors are needed for a wide range of applications such as biomonitoring, cryosurgery, soft robotics, and other flexible electronic applications.[4,5] The most common method of sensing temperature is by measuring thermoelectric voltage generated by two different metal/metal alloy junctions under a temperature gradient (Seebeck effect).[6] The thermoelectric voltage is directly proportional to the applied temperature gradient and can be written as

$$V = S \cdot \Delta T \quad (1)$$

where ΔT is the temperature gradient and S is the Seebeck coefficient. Film-based temperature sensors are used for accurate temperature measurement for various applications ranging from intracellular thermometry[1] to propulsion systems.[6] When placed in a temperature gradient, the same device can also act as an energy harvester.[7,8] Materials used as temperature sensors range from semiconductor metal oxide[9] to metal[10]/metal alloys.[3] However, most of the thin film temperature sensors are manufactured by conventional lithographic methods that require chemical compatibility of the sensor material with the substrate, have a rigid construction, and need high processing temperatures, which makes it difficult to fabricate them on flexible polymer substrates.[3,9] Further, films made from bulk materials are known to be susceptible to channel cracks and localized delamination under bending and/or linear strain.[11] A compelling need thus exists to develop flexible temperature sensors that can sustain the demanding operating conditions encountered in several applications.

Received: April 4, 2019
Accepted: April 9, 2019
Published: April 9, 2019

ACS Publications © 2019 American Chemical Society

DOI: 10.1021/acsanm.9b00628
ACS Appl. Nano Mater. 2019, 2, 3280−3291

Downloaded via CARNEGIE MELLON UNIV on March 08, 2025 at 06:46:59 (UTC). See https://pubs.acs.org/sharingguidelines for options on how to legitimately share published articles.

Printed electronics, an additive manufacturing method, has emerged as a rapid fabrication technique where electronic devices with different 2D and 3D architectures can be realized over arbitrary substrates. Printing allows different materials in nanoparticle form to be deposited onto substrates such as polymers and then sintered at low temperatures to create the functional films.[12−14] Printing involves minimal process steps (e.g., printing and sintering)[15] when compared to lithography or MEMS methods. Further, the use of nanoparticles allows the sintering to happen at relatively low energies,[16−18] which is expected to reduce the potential damage to the underlying substrate. Among different printing methods, aerosol jet printing has been used to fabricate a wide variety of electronic devices such as touch and proximity sensors,[19] biochemical sensors,[20] strain sensors,[21] ring oscillators,[22] solar cells,[13,23] 3D electronic interconnects,[24] gate dielectrics,[12] 3D passives,[25] and 3D antenna structures.[26] In the aerosol jet method, a mist of nanoparticle ink droplets is created through ultrasonic or pneumatic atomizer which is then directed and aerodynamically focused by a carrier gas and sheath gas to print features as small as 10 μm on arbitrary substrates.[27,28] The printed nanoparticles can be sintered using various methods such as microwave,[29] heat,[19,21,26,27] and photonic flash.[30,31,32] We note that the films made by printing and sintering of nanoparticles have shown high resilience to thermal strain in our prior work, which was attributed to the inherent porosity within the film that creates large internal surface areas that cannot support stress[33], which leads to a lower stress build-up for a given strain.[21]

The impetus for the present work is twofold. First, we aimed to use nanoparticles to create a fabrication platform for high performance temperature sensors that can be used for soft robotics,[34] biomedical,[35] energy,[36] industrial,[37] and defense requirements.[38,39] The focus was to develop and optimize the printing processes for copper (Cu) and constantan ($Cu_{50}Ni_{50}$) alloy nanoparticles on Kapton substrate and use low-power laser sintering under a forming gas (5% H_2 in N_2) to prevent burning of the polymer substrate and allow control of particle oxidation. The second aim was to thoroughly characterize the micro- and nanostructure of the films and their effect on device electrical and mechanical performance. The focus was to measure the device repeatability and variability in as-fabricated condition and after repeated mechanical deformation.

2. EXPERIMENTAL SECTION

2.1. Materials and Sensors Fabrication. We printed solvent based Cu and CuNi nanoparticle inks using Aerosol Jet printer (AJ-300, Optomec, Inc., Albuquerque, NM) to realize the two elements/films of the sensor. The Cu nanoparticle ink (IMC-2501 Cu ink, Intrinsiq Materials Inc., Rochester, NY) had a viscosity of about 100 cP, a particle size of 86 ± 4 nm, and a particle loading of 65 wt %. The CuNi nanoparticle ink (OC5050 ink-CuNi, Applied Nanotech, Inc., Austin, TX) had a viscosity of about 50 cP, particle size range of 140−210 nm, and a particle loading of 50 wt % per the manufacturer data sheet. Prior to printing, an AutoCAD schematic (Autodesk Inc., San Rafael, CA) was fed to the 3D printer. Note that the Aerosol Jet printer allows the deposition of nanoparticles dispersed in a solvent (i.e., nanoparticle ink) onto a substrate by creating a mist of droplets with sizes of 1−5 μm (each droplet containing multiple nanoparticles).[40] The droplets are guided by a carrier gas (N_2) followed by a sheath gas (also N_2) to create an aerodynamically focused jet. The primary components of the Aerosol Jet printing system include two atomizers (ultrasonic and pneumatic), a programmable *XY* motion stage, and a deposition head. An additional laser system was used to sinter the nanoparticle films under a shroud of forming gas (5% H_2 in N_2).[41] The process parameters used during deposition of Cu and CuNi nanoparticle inks in this work are given in Table 1. The sensors were printed using one layer of deposited ink with individual electrodes formed by 10 lateral (i.e., side-by-side) passes to achieve a line width of about 600 μm. During printing, the standoff distance between the substrate and the nozzle was kept at about 5 mm. Note that the optimized parameters such as sheath gas pressure, atomizing pressure, and exhaust pressure were suitable for the ink formulation used in the current work but can differ for other inks depending upon their viscosity, particle size, and the solvents used.

Table 1. Printing Parameters of Cu and CuNi Allow Nanoparticle Ink

parameter	Cu	CuNi
nozzle diameter (μm)	300	300
atomizer flow (sccm)	950	950
exhaust VI flow (sccm)	900	910
sheath gas (N_2) flow (sccm)	50	50
platen temp (°C)	60	60
process speed (mm/s)	10	10

Figure 1 shows the schematic of the substrate preparation and nanoparticle printing and sintering processes. The substrates (Kapton) were first washed with deionized (DI) water and isopropyl alcohol (IPA) followed by Ar/O_2 plasma treatment for 5 min (PICO UHP RF, Diener Electronic, Ebhausen, Germany) prior to nanoparticle printing. The printed nanoparticle films were sintered after printing was completed by an IR laser at 100 mW and 400 mW power rastering at a speed of 10 mm/s over the Kapton tape. The laser spot size was 50 μm. Note that the power and speed used in the current experiments was determined after an optimization of these parameters. For example, low laser power and high speed did not result in enough sintering, while high laser power with low rastering speed resulted in black burn marks indicating excessive metal oxidation and/or degradation of the polymer. A suitable processing window was identified at 10 mm/s laser rastering speed and between 100 mW and 400 mW power. Note that the printing also happens at 10 mm/s (Table 1). The total time for printing and sintering per device (e.g., for 10 cm long sections of Cu and CuNi with about 6 passes per section) is thus of the order of a few minutes. This speed of device fabrication is highly compatible with roll-to-roll manufacturing methods that can lower cost and enable system level integration and mass manufacture of electronic systems.[42] Some of the sensors were coated with silicone protective layer (Dow Corning 3-1953, Midland, MI, USA), also printed by the Aerosol Jet machine to protect the sensor from oxidation and thereby extend the range of sensor usage.

2.2. Sensor Performance Measurement. To measure the sensor output at different temperatures, a four-wire probing method was adopted. A silver based conductive epoxy (Pyro-duct 597-a, Aremco, Valley Cottage, NY) was used to connect the wires with the samples. Conductive epoxy was cured overnight under ambient conditions followed by heat curing at 93 °C for 2 h. Sensors fabricated with 100 mW laser power and 10 mm/s scanning speed had a resistance of ~300 Ω (for the dimensions of the sensor), while the sensors made using 400 mW laser power and 10 mm/s scanning speed had a resistance of 125 Ω for the identical dimensions. The sensor output was measured in terms of dc voltage using a $7_{1/2}$ digit precision multimeter (Keysight 34470A, Santa Rosa, CA). During the measurement, one end of the sample was placed on the hot plate and the other kept under ambient conditions to create a temperature gradient between two ends of the sensor. Commercial thermocouples were placed near the printed sensor's hot and cold junctions to independently record their temperatures.

2.3. Sensor Film Characterization. The morphology of the sensor films was characterized using 3D optical profilometers (Zygo NewView 7300 Middlefield, CT, and Alicona Infinte Focous, Raaba/Graz, Austria), along with scanning electron microscopy (SEM). The surface of sensor films was investigated using X-ray photoemission

DOI: 10.1021/acsanm.9b00628
ACS Appl. Nano Mater. 2019, 2, 3280−3291

Downloaded via CARNEGIE MELLON UNIV on March 08, 2025 at 06:46:59 (UTC). See https://pubs.acs.org/sharingguidelines for options on how to legitimately share published articles.

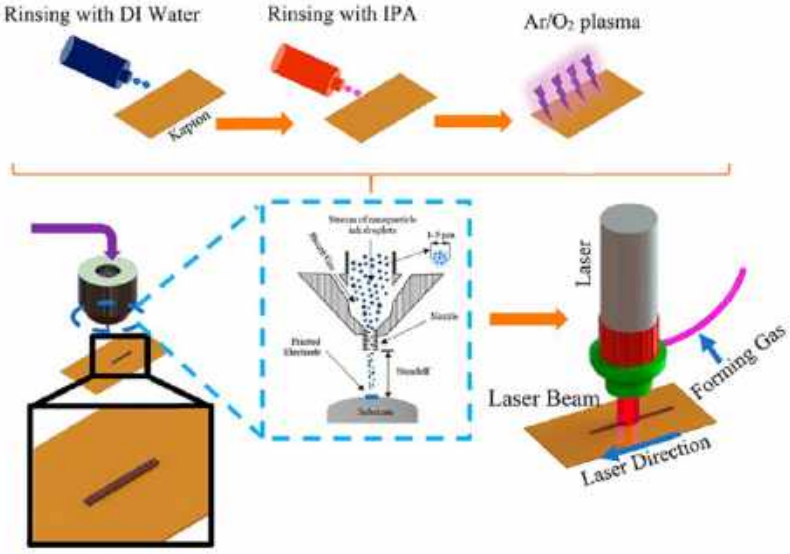

Figure 1. Schematic of the substrate preparation and Aerosol Jet printing process of the Cu/CuNi flexible temperature sensor.

spectroscopy (XPS) using a Thetaprobe (ThermoFisher, Waltham, MA). XPS spectra were obtained using a 400 μm spot size and 200 eV analyzer pass energy with the sample at room temperature. The base pressure during XPS measurements was $<10^{-8}$ Torr. The particle coalescence and bonding to the substrate were measured using focused ion beam or FIB (FEI Scios dual beam FIB/SEM machine) followed by transmission electron microscopy (TEM). We also used selective area electron diffraction (SAED) inside the TEM to identify the phases present in the sensor films after sintering.

3. RESULTS AND DISCUSSION

3.1. Morphology of Printed Films. Figure 2 shows CAD schematic and optical images of the flexible temperature sensors at different magnifications. A pair of large pads (~1 mm × 1 mm) were also printed at the ends of the sensor for electrical contacts for external measurements. A higher magnification image of the representative sensor in Figure 2c,d indicates a uniform edge in all the regions. The electrode width variation for the Cu film was measured at about 40 locations under an optical microscope and showed a mean width of 602.4 μm and a variation of ±7.8 μm, or 1.3% of the mean (Figure 3a). The electrode width variation for the CuNi film was also measured at 40 locations under an optical microscope and showed a mean width of 561.9 μm and a variation of ±6.0 μm, or 1.07% of the electrode width (Figure 3b). The low variation of electrode width in Figure 3 indicates uniformity of the Aerosol Jet printing process. The 3D profilometer scans of the Cu film, shown in Figure 3c,d, indicate an average height of about 2 μm but considerable height variation for the different passes. A similar plot for the CuNi film is shown in Figure 3e,f with an average height of about 2.5−3 μm. As will be shown in section 3.3, the variability in the film dimensions shown in Figure 2 did not affect the sensor performance since the voltage resulting from the Seebeck effect depends only upon the material and the temperature gradient (eq 1).

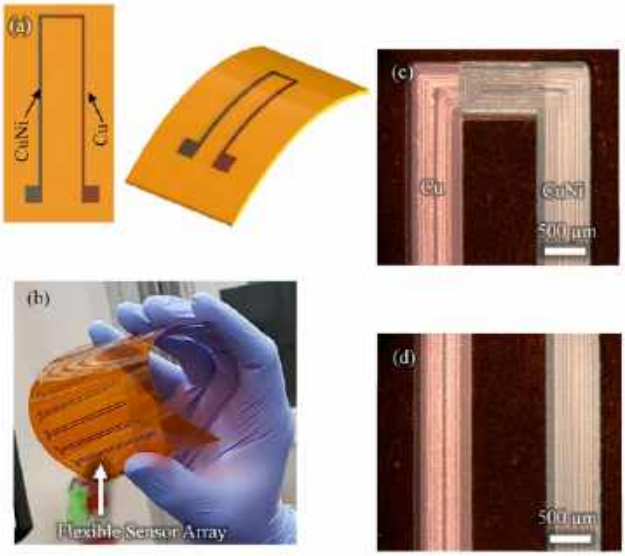

Figure 2. Schematic and optical images of the printed flexible temperature sensors. (a) Schematic of the sensor showing top and flexed views. (b) Optical image of an array of printed sensors on Kapton substrate. (c, d) Optical images of the sensor at different locations.

3.2. Micro- and Nanostructure of Printed Films. *3.2.1. Surface Morphology by SEM.* The different laser powers used in this study are expected to lead to different microstructures and porosity levels. Parts a and b of Figure 4 show representative SEM images of the Aerosol Jet printed Cu nanoparticle films sintered at 100 mW and 400 mW laser power at 10 mm/s scanning speed, respectively. The same surfaces at a lower magnification are shown in Figure S1a,b in the Supporting Information. The film surface has periodic surface voids shown in Figure 4a with the nanoparticles fused with each other at both laser powers. The higher laser power sample shown in Figure 4b, however, shows a higher degree of sintering. We note that CuNi has a higher melting temperature (~1250 °C) than Cu (1085 °C). We thus expected the degree of sintering to be marginally lower for CuNi than Cu. Indeed as shown in Figure 4c,d, we qualitatively observe that the CuNi nanoparticles under identical sintering conditions show a higher degree of porosity than Cu. The CuNi surfaces at a lower magnification are shown in Figure S1c,d in the Supporting Information.

DOI: 10.1021/acsanm.9b00628
ACS Appl. Nano Mater. 2019, 2, 3280−3291

Downloaded via CARNEGIE MELLON UNIV on March 08, 2025 at 06:46:59 (UTC). See https://pubs.acs.org/sharingguidelines for options on how to legitimately share published articles.

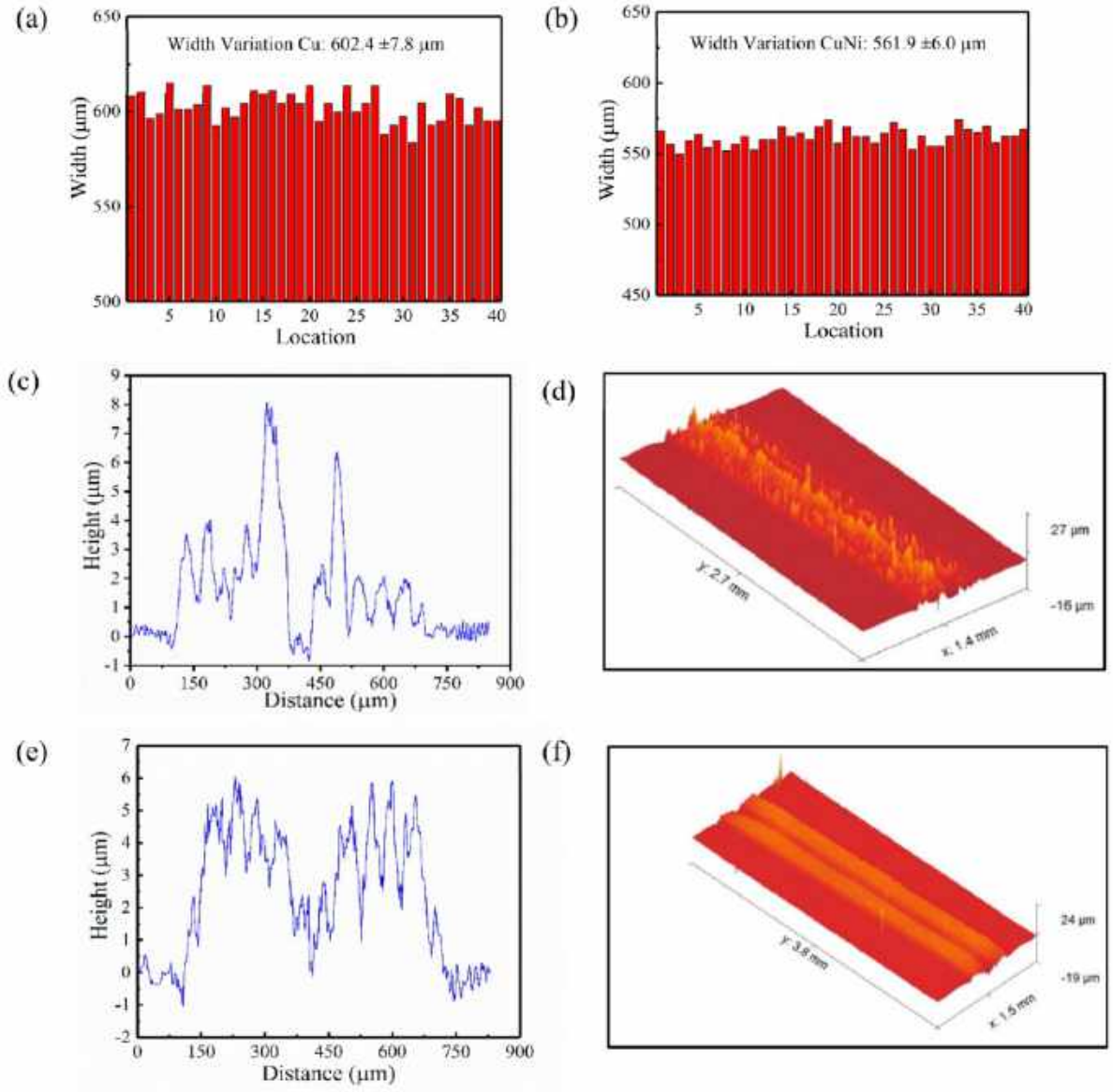

Figure 3. (a) Width variation of the printed Cu film at different region. Variation of the width is about ±7.8 μm from the mean, i.e., 1.2% from the mean. (b) Width variation of the printed film at different region. Variation of the width is about ±6.03 μm from the mean, i.e., 1.2% from the mean, indicating high printing accuracy of the Aerosol Jet system. (c) Surface topology of the printed Cu with an average height of approximately 2.5 μm, (d) 3D profilometer scan of the printed Cu element. (e) Surface topology of the printed CuNi with an average height of approximately 4 μm. (f) 3D profilometer scan of the printed CuNi element.

The presence of porosity for films made by sintering of nanoparticles is well-known and depends upon the energy supplied to the film in addition to the starting nanoparticle sizes.[43,44] Copper nanoparticles sintered by intense laser power showed a porosity of about 13%,[45] while thermal sintering of Cu−Ni nanoparticles in a reducing atmosphere between 300 and 800 °C showed a porosity in the range of 10−20% in the images presented in that work.[46] The porosity in Figure 4 and the section in Figure 5 are within about 10−24% of the bulk (see Figure S2a−d in the Supporting Information), and within the range of that obtained by other sintering methods mentioned above.[45,46] Note that for unsintered films, the nanoparticles are not connected to one another and are mixed with binders precluding us from defining the porosity in that state. From a manufacturing perspective, it is desirable to sinter the film using lower laser power as it will help to protect the underlying polymer substrate (whose damage also depends on the laser scanning speed) and lower the manufacturing cost. Of course, there needs to be sufficient degree of sintering for the device to function properly. First, for none of the process parameters used in this study (Table 1) did the Kapton substrate exhibit any visible surface damage; implying that both of the process conditions can be used to fabricate the device. Further, as discussed in section 2.2, the combined resistance of the device (consisting of Cu and CuNi sections) was about 300 Ω for 100 mW laser power and 10 mm/s scanning speed and about 125 Ω for 400 mW laser power and 10 mm/s scanning speed. The ability to generate EMF in the sensor is independent of the resistance of the metal wire. As a result, it is expected that the two sintering powers should not significantly

DOI: 10.1021/acsanm.9b00628
ACS Appl. Nano Mater. 2019, 2, 3280−3291

Downloaded via CARNEGIE MELLON UNIV on March 08, 2025 at 06:46:59 (UTC). See https://pubs.acs.org/sharingguidelines for options on how to legitimately share published articles.

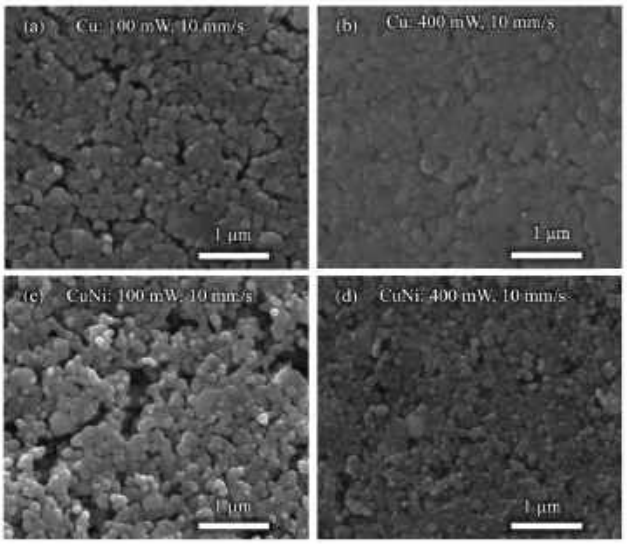

Figure 4. Representative SEM images of the Aerosol Jet printed Cu and CuNi nanoparticle films. (a, b) Surface morphology of the Cu film sintered at 100 mW and 400 mW laser power and 10 mm/s scanning speed, respectively. Periodic surface voids from sintering porosity are observed at 100 mW power. The film is denser when sintered at the higher power. (c, d) Surface morphology of the CuNi film sintered at 100 mW and 400 mW laser power and 10 mm/s scanning speed, respectively. Compared to Cu, the degree of sintering is lower with large cracks running throughout the film. A more uniform CuNi film is formed at 400 mW laser power and 10 mm/s scanning speed. Images of the sintered surfaces at lower magnification are given in Figure S1 in the Supporting Information.

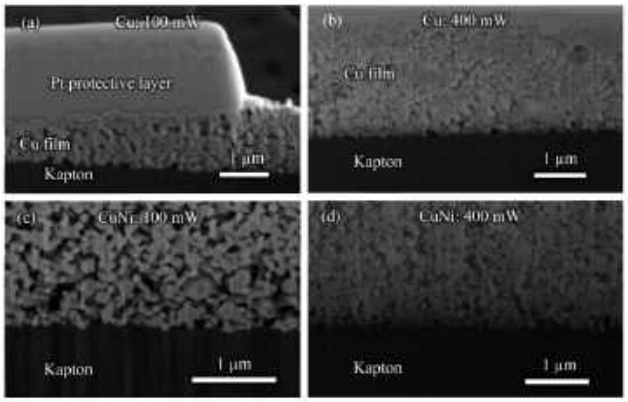

Figure 5. FIB/SEM images of sintered Cu and CuNi films sintered by lasers with different powers: (a) cross-sectional image of the Cu film sintered at 100 mW laser power; (b) cross-sectional image of the Cu film sintered at 400 mW laser power; (c) cross-sectional image of the CuNi film sintered at 100 mW laser power; (d) cross-sectional image of the CuNi film sintered at 400 mW laser power. Both Cu and CuNi films show less porosity and better calescence at 400 mW laser sintering power.

affect the performance of the sensor as will be demonstrated in section 3.3.

3.2.2. Film Cross Section by FIB. To gain further insight into the microstructure through the film thickness, we cross-sectioned the films in a FIB/SEM machine and observed the internal porosity. Figure 5 shows FIB/SEM cross-sectional images of sintered Cu and CuNi films at different magnifications and laser sintering powers but with the same sintering speed of 10 mm/s. Parts a and b of Figure 5 show the cross-sectional images of the Cu films sintered at 100 mW and 400 mW laser power, respectively. We note that the FIB process can heat the film locally (with spot size of the order of 10s of nm across) with the temperature rise being inversely proportional to the thermal conductivity (κ) of the film material.[47] The increase in local temperature due to FIB for Cu (~400 W/(m·K)) and CuNi (~20 W/(m·K)) is expected to be <1 °C and ~15 °C above the ambient, respectively.[47,48] This temperature rise is not significant to affect the sintering process, and we expect that the images in Figure 5 are representative of the film microstructure after laser sintering. We note that the thickness of the film in Figure 5a is lower than that in Figure 5b. In reality, it is expected that when using a higher laser power, the Cu film will have a higher density, and the thickness should be less than the one processed with lower laser power. The printing height variation shown Figure 3c,e is high, however, which precluded us from doing a systematic study of the thickness change of the printed nanoparticle films due to the two laser sintering processes.

It is clear from parts a and b of Figure 5 that the heat deposited by the laser penetrated and caused sintering throughout the film thickness of several microns in both of the cases. This result is very important from manufacturing perspective and indicates that the low-power laser sintering method is sufficient to create films with several micrometer thickness from a bed of nanoparticles on a polymer substrate. Second, the film sintered at lower laser power shows higher porosity, consistent with the surface observations shown in Figure 4. Similar results are shown in parts c and d of Figure 5 for CuNi nanoparticle films.

3.2.3. Film Internal Structure and Interface Architecture by TEM and SAED. To gain insight into the degree of sintering of the nanoparticles as well as the phases formed, we observed the films under TEM and SAED. The TEM sample preparation process is shown in Figure S3 and described in section S1 of the Supporting Information. Parts a and b of Figure 6 show representative TEM images of the Cu film sintered at 100 mW laser power and 10 mm/s scanning speed at different magnifications. The Cu grains are spherical with a grain size of ~106 ± 21 nm. The images reveal that the grains are fused together during laser sintering through the film thickness. The calculated necking radius of the fused particles is about 81 ± 16 nm. This gives the neck length to diameter ratio (X/D) of about 0.76, which represents the degree of sintering in the Cu film with 100 mW laser power (X/D = 1 indicates fully sintered nanoparticles). No distinct oxide layer was observed in the TEM images (15 images analyzed). We also note that the film particles are well adhered to the Kapton substrate without any interface cracks with a zone of interpenetration of up to 20 nm.

Figure 6c shows the SAED patterns of the Cu nanoparticles film. The ring-shaped diffraction patterns suggest the presence of randomly oriented nanocrystals which agrees with the TEM images shown in Figure 6a,b. The SAED pattern shows strong reflections close to those of Cu. However, fewer diffraction spots for Cu (002) and (113) planes compared to Cu (111) and (002) planes indicate that the particles are preferentially oriented in certain directions. In addition, diffraction spots for CuO (002) and CuO (202) plane were also observed. This is in spite of the fact that no distinct oxide layer was observed at the particle surfaces in the TEM image of Figure 6a,b. We note that there may be some oxide on the Cu nanoparticles in the

DOI: 10.1021/acsanm.9b00628
ACS Appl. Nano Mater. 2019, 2, 3280−3291

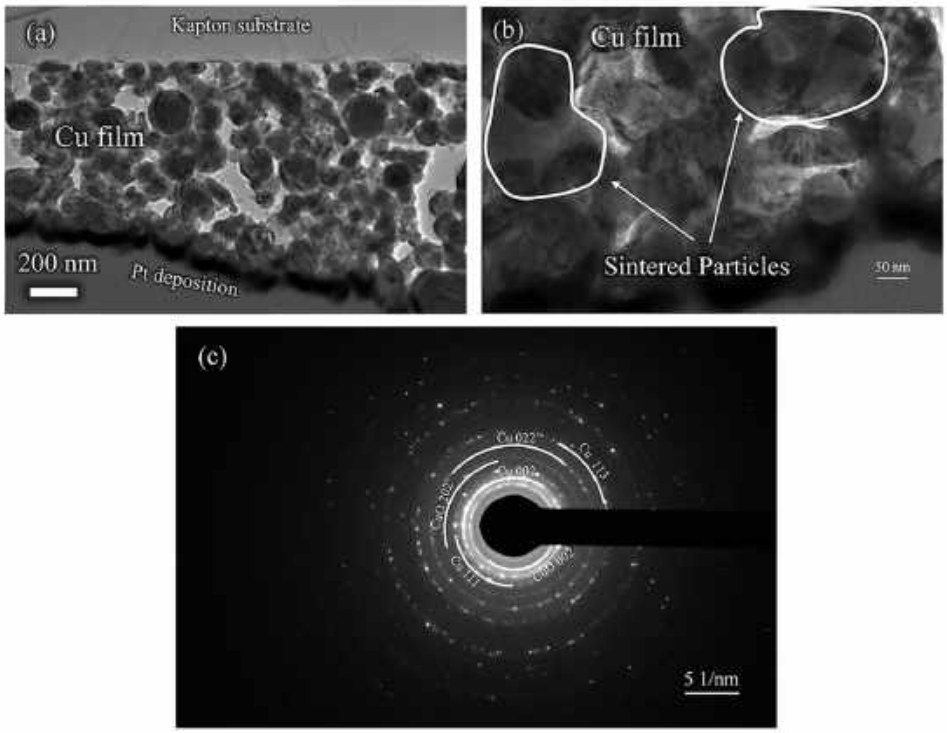

Figure 6. (a) TEM image of the Cu lamella showing sintered nanoparticle film and substrate at different magnifications. The film was sintered at 100 mW laser power and 10 mm/s scanning speed. (b) Higher magnification image shows that the nanoparticles have properly fused together during laser sintering. (c) Selective area electron diffraction image of the Cu nanoparticle film showing existence of Cu major planes.

inks even before they are sintered. These results, however, indicate that minimal oxidation occurred during the manufacturing process. As will be shown later, the sensor performance was not affected by this observation.

Parts a and b of Figure 7 show the TEM images of the laser sintered CuNi film and its interface with the Kapton substrate. The CuNi grain size was ~149 ± 34 nm, and the grains were fused/sintered together. Some outliers (large particles ~426 nm.) were also observed in the sintered film as shown in Figure 7c. The TEM images in Figure 7a,b also reveal that the grain morphologies sintered by laser power are approximately equiaxed but not spherical. The calculated necking radius of the fused nanoparticles is about 65 ± 14 nm. After sintering, the X/D ratio is about 0.44. This indicates completion of the initial stage of sintering and beginning of intermediate stage sintering when 100 mW laser power is used. The X/D ratio for CuNi is lower than that for Cu, which may be a result of its higher melting temperature compared to Cu, which results in a higher stability of CuNi nanoparticles when subjected to laser power. The film was well adhered to the Kapton substrate with no evidence of interfacial cracking, a result similar to that for Cu as shown in Figure 6. The porosity of the TEM images in Figures 6 and 7 can explain the higher resistance of the sensors sintered at 100 mW than that of films sintered at 400 mW. This difference, however, did not affect the sensitivity of the sensors as discussed in section 3.3.

To look at the crystal structure for CuNi during sintering, we carried out selective area electron diffraction (SAED) analysis of the samples. Figure 7c shows the diffraction patterns of the CuNi nanoparticle films after sintering. The ring-shaped diffraction pattern suggests the presence of randomly oriented nanocrystals, which agrees with the TEM images shown in Figure 7a,b. The CuNi alloy showed phase of CuNi (1/1) which is similar to manufacturer specification of overall Cu and Ni concentration. The pattern also shows strong reflection close to the CuNi (111) and (002) planes. In addition, diffraction spots for the CuNi (022) plane were observed; however the number of spots was fewer than for CuNi (111) and (002) indicating that the particles are preferentially oriented in a certain orientation. The SAED pattern in Figure 7c shows a finite width for the diffraction rings, indicating that the lattice parameters have a range of values, which has been observed in agglomerated nanoparticles.[49] In the present case, large surface areas of the fused nanoparticles (Figure 7a,b) are likely to cause the diffuse rings.

3.2.4. Chemical State of Cu and Ni Surfaces. To further investigate the oxidation of the films, XPS measurements were used on the Cu and CuNi films sintered with 400 mW (Figure 8) and 100 mW (Figure S4) laser powers. XPS probes the Cu 2p, Ni $2p_{3/2}$, and O 1s core levels to determine their binding energies. The Cu LMM Auger peak was also obtained to distinguish Cu oxidation states on both Cu and CuNi films. Figure 8 top row shows the Cu 2p, Ni $2p_{3/2}$, O 1s XP spectra and the Cu LMM Auger peak for the CuNi film sintered with 400 mW laser power. The binding energies are 953 eV for Cu $2p_{1/2}$ and 933 eV for Cu $2p_{3/2}$.[50] There is no satellite feature between the Cu 2p XP peaks indicating that Cu is not oxidized. The Cu LMM Auger peak at the kinetic energy of 918.6 eV for the CuNi film also demonstrates that Cu is in metal form.[50] The XPS signal for Ni $2p_{3/2}$ is weak and not well resolved; therefore, we cannot conclude whether Ni is oxidized or not. The reason for the weak Ni $2p_{3/2}$ peak might be surface segregation of Cu in the CuNi film as reported in some prior experimental and theoretical studies on Cu−Ni alloys.[51−56] Cu has a lower surface free energy than Ni; therefore, it is expected to segregate to the surface of the alloy film.[56] The O 1s XP

DOI: 10.1021/acsanm.9b00628
ACS Appl. Nano Mater. 2019, 2, 3280−3291

Downloaded via CARNEGIE MELLON UNIV on March 08, 2025 at 06:46:59 (UTC). See https://pubs.acs.org/sharingguidelines for options on how to legitimately share published articles.

Downloaded via CARNEGIE MELLON UNIV on March 08, 2025 at 06:46:59 (UTC). See https://pubs.acs.org/sharingguidelines for options on how to legitimately share published articles.

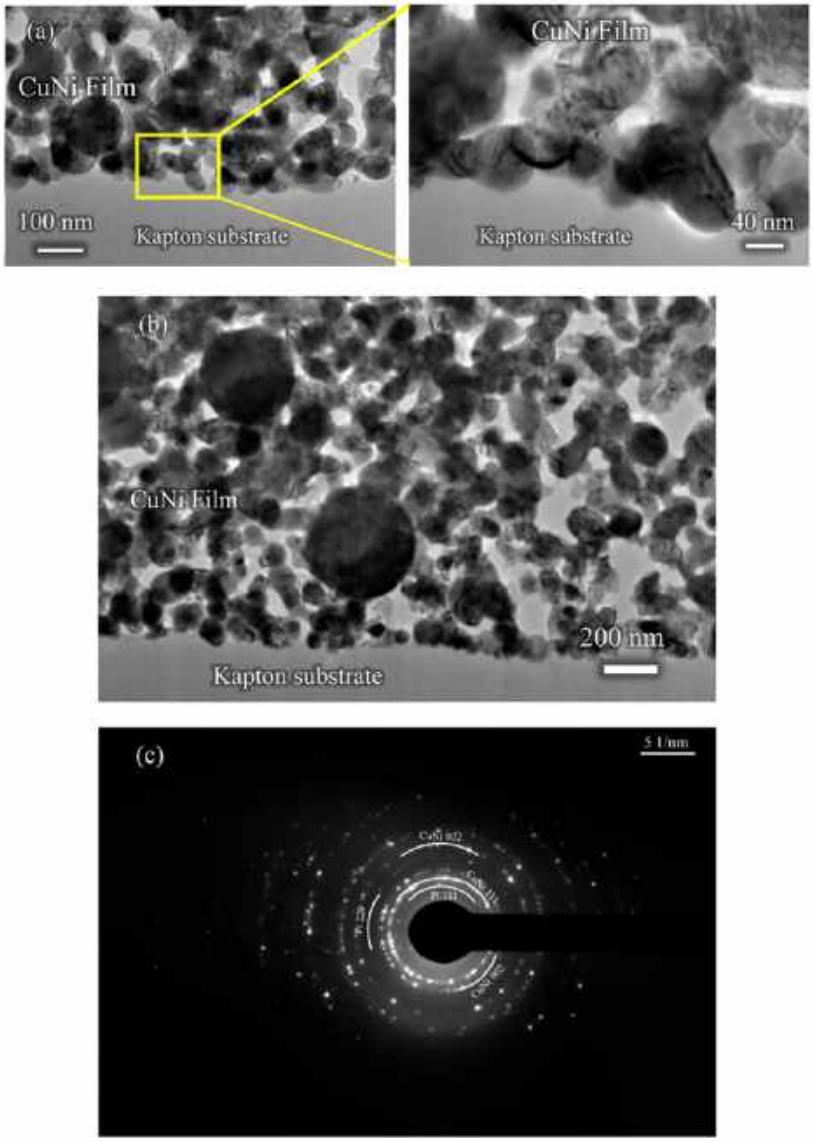

Figure 7. (a) TEM image of the CuNi lamella showing nanoparticle film and substrate. Higher magnification image shows that the nanoparticles have properly fused together during laser sintering. (b) TEM image showing outliers having diameter of ~426 nm. (c) Selective area diffraction image of the CuNi nanoparticle film. The image shows existence of CuNi major planes. In addition, few diffraction spots are also observed from Pt which was deposited on the top surface of the film as a protective layer.

spectrum contains one peak at 532 eV. Figure 8 bottom row shows the Cu 2p, Ni $2p_{3/2}$, O 1s XPS and Cu LMM Auger peak for the Cu film sintered with 400 mW laser power. The Cu peaks at binding energies of 953 and 933 eV correspond to the Cu $2p_{1/2}$ and Cu $2p_{3/2}$ levels, respectively.[50] The weak satellite peak at 945 eV indicates the existence of Cu(I) oxide (Cu_2O) on the Cu film.[50] The Auger peak at the kinetic energy of 916.6 eV for Cu LMM also demonstrates the presence of Cu_2O on the Cu film.[50] There are no Ni $2p_{3/2}$ peaks in the XP spectrum of the Cu film, as expected. For O 1s, there is only one peak at binding energy of 532 eV. These results show that no surface oxidation was detected for CuNi films, while Cu film showed the presence of surface oxide.

3.3. Sensor Device Testing. *3.3.1. Sensor Performance.* We evaluated the performance of the temperature sensors sintered using 100 mW and 400 mW laser power and 10 mm/s scanning speed. Figure 9 shows thermoelectric output of the sensors. Thermoelectric response was recorded for at least three thermal cycles for six samples. Initially, the sensors were characterized up to 140 °C with and without the silicone protective layer on top. Figure 9a shows thermoelectric output of six sensors, recorded three times each as a function of temperature (sensors 1−3 were sintered using 400 mW laser, while sensors 4−6 were sintered using 100 mW laser). It is clear that the sensor output voltage is linear as a function of temperature. Further, the sensor measurements (spread over several days) were repeatable with minimal temperature drift. It is observed that, as expected, the silicone protective layer (sensor 1) did not affect the sensor performance. The protective layer also did not delaminate for this temperature range. The Seebeck coefficient of the sensors were 40.02 ± 0.22, 38.93 ± 0.24, 39.92 ± 0.18, 40.07 ± 0.23, 40.03 ± 0.23, 40.01 ± 0.19 μV/°C, with an overall mean and standard deviation of 39.83 ± 0.273 μV/°C. The sensor performance

DOI: 10.1021/acsanm.9b00628
ACS Appl. Nano Mater. 2019, 2, 3280−3291

Downloaded via CARNEGIE MELLON UNIV on March 08, 2025 at 06:46:59 (UTC). See https://pubs.acs.org/sharingguidelines for options on how to legitimately share published articles.

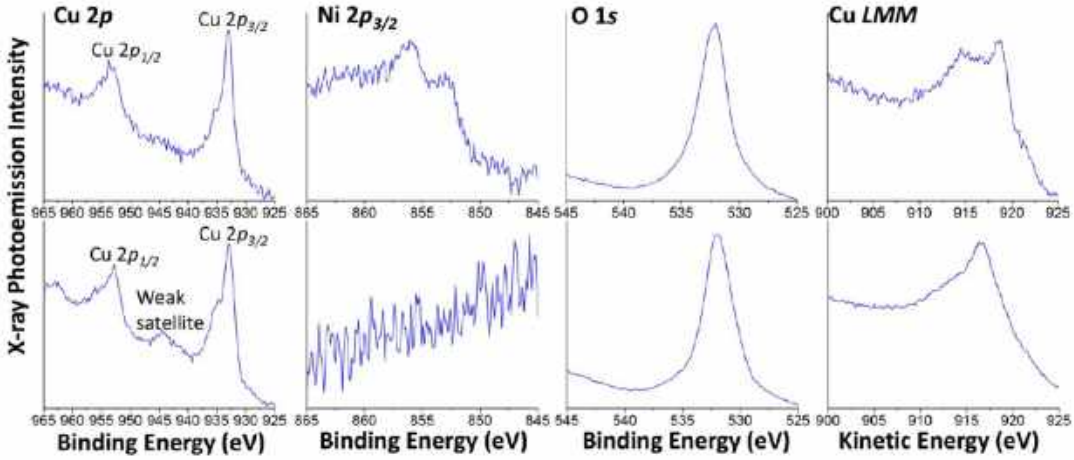

Figure 8. Cu 2p, Ni $2p_{3/2}$, O 1s XPS and Cu LMM Auger spectra for CuNi (top row) and Cu films (bottom row) sintered with 400 mW laser power. For the NiCu film, the Cu 2p XP and Cu LMM Auger spectra indicate that Cu is not oxidized. The Cu 2p XP and Cu LMM Auger spectra for the CuNi film indicate some Cu oxidation.

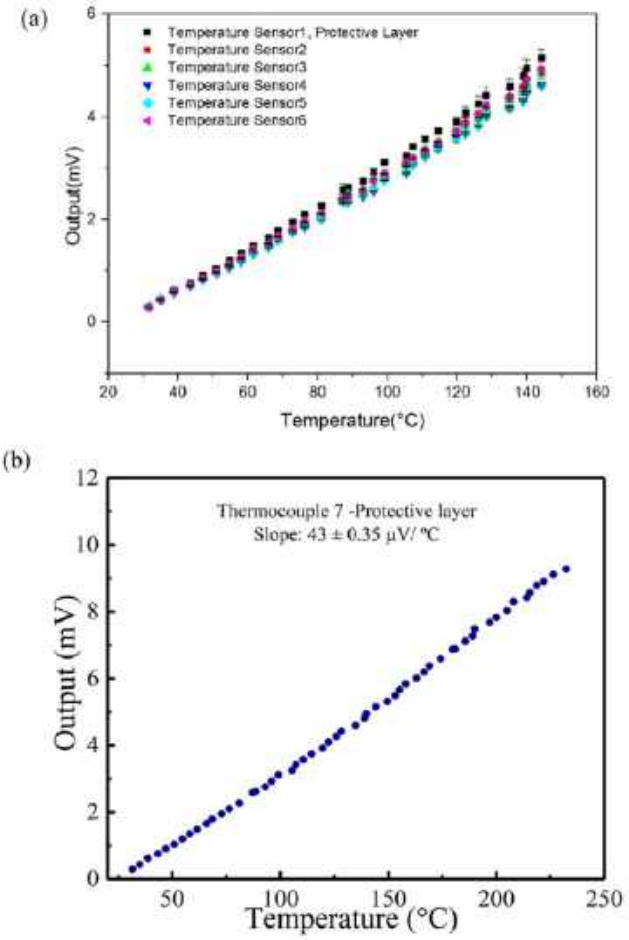

Figure 9. (a) Thermoelectric output as a function of temperature up to 140 °C for six temperature sensors. The protective layer does not affect the sensor characteristics. Sensors 1−3 were sintered using 400 mW laser, while sensors 4−6 were sintered using 100 mW laser. The variation in the slope of the curves for all the data combined is 39.8 ± 0.273 μV/°C. (b) Thermoelectric output as a function of temperature up to 232 °C for one sample with protective layer.

was thus highly repeatable and linear for the two process conditions and the existing variation in the sensor dimensions.

For the sample coated with silicone protective layer, the thermoelectric response was recorded up to 232 °C (Figure 9b), and the calculated Seebeck coefficient was ~43.68 ± 0.35 μV/ °C. The highest thermoelectric power recorded for this sample is 9.27 mV. Only one set of data was recorded for this sample as it showed heavy wrinkling due to poor adhesion and/or thermal expansion mismatch between the sensor film and the protective layer. Note that wrinkling and delamination were observed mostly on the Cu film rather than the CuNi film. Figure S5a of the Supporting Information shows 3D profile of the delamination with wrinkle height of up to 90 μm after the high temperature measurement (Figure S5b). It is unclear why the protective layer had poorer adhesion to Cu than CuNi, but we speculate that some additional oxidation may have happened at Cu−silicone interface due to oxygen diffusion, weakening that interface.

We note that the temperature sensors in this study showed better sensitivity compared to any other film-based temperature sensors reported in the literature. For example, flexible temperature sensors based on Ir and Ir−Rh wires showed a Seebeck coefficient (i.e., sensitivity) of 5.9 μV/°C.[3] The same parameter of Pd/Cr based sensors developed by Yang et al.[2] was 20.99 ± 0.1 μV/°C. Other noble metals such as Au/Pd showed very low Seebeck coefficient of around 1.18 μV/°C.[1] The Seebeck coefficient of ~40 μV/°C for the sensors in this work is double that of the highest sensitivity yet reported for film-based sensors.[1−3]

As seen in Figure 9, the two sintering conditions considered in the current work did not affect the sensor performance. Further, the high variation in the sensor film height (Figure 3c,e) did not affect the sensor performance. This can be explained as below. The thermoelectric output of the sensor is related to the temperature gradient between the junctions and the Seebeck coefficient (eq 1), which depends only upon the particular material set used to construct the sensor. The height variation will give rise to a variation in resistivity and hence only a drop in current through the device (but not the voltage). The effective resistivity of the films was estimated to be about 3−6 times that for the bulk and is quite low. The performance of the sensor was thus not affected by the height

DOI: 10.1021/acsanm.9b00628
ACS Appl. Nano Mater. 2019, 2, 3280−3291

Downloaded via CARNEGIE MELLON UNIV on March 08, 2025 at 06:46:59 (UTC). See https://pubs.acs.org/sharingguidelines for options on how to legitimately share published articles.

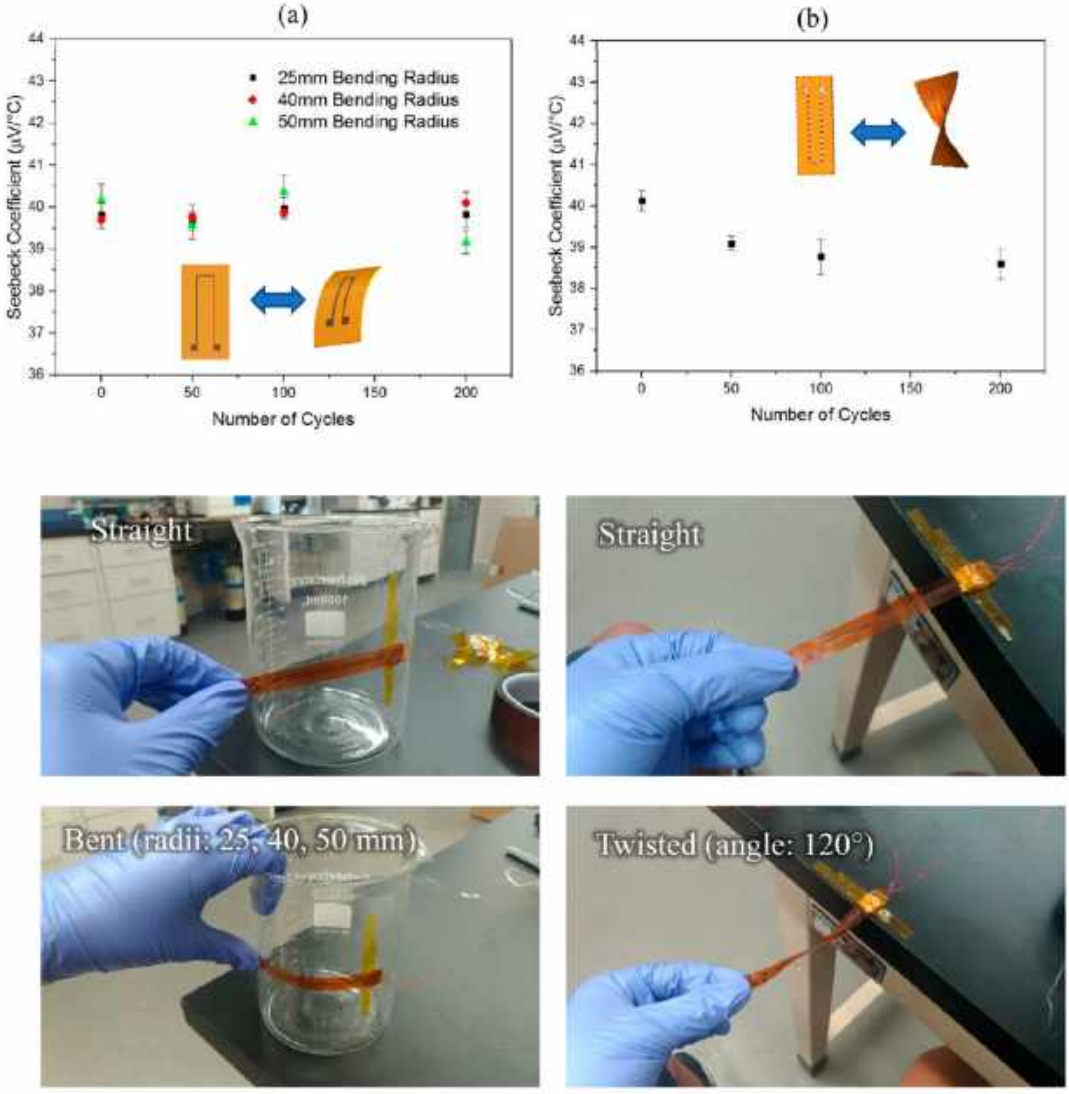

Figure 10. Flexibility test for the temperature sensor. (a, left) Bending test showing the Seebeck coefficient of the sensor within the range for initial tests after 200 cycles. (b, right) Twisting test showing only marginal reduction in Seebeck coefficient at about 2.5% of the initial tests after 200 cycles.

variation. The above result has important implications for the use of nanomaterials to fabricate electronic devices. For example, the result will lead to lowering of the cost of manufacture as highly uniform films are *not required* to get a better device performance. This will lower the cost of quality control and help with the adoption of nanoparticle based fabrication methods for such electronic devices.

3.3.2. Sensor Flexibility Test. In order to assess the viability of the sensors under demanding loading conditions, we carried out bending and twisting tests for the temperature sensors we fabricated. Three bending conditions were used with bending radii of 25 mm, 40 mm, and 50 mm (around a glass flask) and then straightened for 200 cycles. The sensor performance (thermoelectric output as a function of temperature up to 140 °C) was measured initially and then after 50, 100, and 200 cycles. In addition, a different set of sensors were twisted to an angle of 120° and the performance was measured initially and then after 50, 100, and 200 cycles. Parts a and b of Figure 10 show the initial sensor performance and that after 50, 100, and 200 cycles of bending and twisting, respectively. The test setup for the bending and twisting cycles is also shown in Figure 10. The flask ensured a constant radius for each bending cycle. The sensor twisting was done manually with an estimated angle of twist within about 120 ± 2°. In the case of bending, the sensor performance was within the range of initial data, indicating minimal damage to the sensor after the test. In the case of twisting stress, the Seebeck coefficient degraded only marginally (2.5% degradation) with respect to the initial observations. Optical inspection of the film after 200 bending and twisting cycles showed no visible cracks or delamination (Figure S6).

We explain the lack of sensor degradation under repeated mechanical loads as follows. Bulk mechanical films on polymer show rapid stress build-up under twisting and bending stresses.[11] The porous films in this study, however, are expected to be more strain tolerant because porosity offers free surfaces within the volume of the film that cannot support stress. Further, the fused nanoparticles seen in Figures 6 and 7 can act as micro- and nanoscale springs,[57] softening the film by lowering its effective elastic modulus by as much as an order of

DOI: 10.1021/acsanm.9b00628
ACS Appl. Nano Mater. 2019, 2, 3280−3291

Downloaded via CARNEGIE MELLON UNIV on March 08, 2025 at 06:46:59 (UTC). See https://pubs.acs.org/sharingguidelines for options on how to legitimately share published articles.

magnitude when compared to the bulk values.[44,58] This softening allows the film to support a large strain without a proportional build-up of the stresses in the system,[59,60] thus avoiding cracking or delamination under bending and twisting cycles. Note that such strain tolerance has been achieved in literature by others using cracked gold films on soft polymer substrates.[61] Note also that our previous work has shown that printed and sintered films demonstrate higher apparent Poisson ratio and lower thermal strain at temperatures up to 500 °C.[21]

The work presented in this paper accomplishes the design and manufacture of nanoparticle-based highly flexible linear temperature sensors that show a "high performance" as measured by the sensor sensitivity (highest for film-based sensors), repeatability of sensor performance under different manufacturing conditions (Figure 9), and sensor flexibility under bending and twisting cycles (Figure 10). The unified picture of process and device characterization advances our knowledge of the fascinating area of the bottom-up manufacture of electronic devices on flexible substrates. The manufacturing method allows the sensors to be printed at a rapid speed. For example, the printing and sintering speeds of 10 mm/s (Table 1) allow the fabrication of the sensor shown in Figure 2 in a few minutes. The sensors can be fabricated anywhere, including over a flexible, curved, and angled surface for integration with other active and passive electronic devices. Alternatively, the sensors can also act as flexible power generation devices if placed under a temperature gradient. Note that we chose Kapton, a thermoset, for the temperature sensor because of the stability of the polymer needed for the range of operation for the sensor itself. Creating nanoparticle films on low-temperature thermoplastic substrates will be part of a future investigation. We also note that the method can be applied to create ceramic films but will require a higher laser power than that used in the current work, which will require appropriate substrate materials. Further, the work will facilitate embedded sensors for large mechanical parts. For example, an insulating Kapton layer can be deposited on the large metal part (using printing[62] or other methods) followed by the temperature sensors. Finally, the speed of fabrication and superior device performance presented in this paper will help overcome the barriers to the adoption of nanotechnology in practical device applications.

4. CONCLUSIONS

(a) A nanoparticle-based fabrication method that uses 3D printing and low-power laser sintering under a shroud of forming gas (5% H_2 in N_2) is developed and optimized to fabricate flexible Cu/CuNi temperature sensors on Kapton substrates.

(b) The microstructure of the films forming the sensor was investigated extensively using SEM, FIB, TEM, SAED, and XPS. Fused nanoparticles with porosity in the range of 9−25% through the thickness of the film were observed that reduced with an increase in laser power. For CuNi films, Cu had segregated on the surface as observed previously in the literature.[56] The TEM images along with SAED and XPS showed minimal oxidation, with no surface oxide phase for the CuNi film but the presence of an oxide phase for the Cu film.

(c) The nanoparticle-based sensor devices demonstrated a superior performance when compared to the current state of the art devices made using bulk fabrication processes. Specifically, the sensors showed a highly linear performance with the highest sensitivity for any film-based temperature sensors in the literature.[1−3] In addition, the sensor sensitivity was repeatable to within ±1% across the two manufacturing conditions and the variation in the device dimensions. Lastly, the sensor performance was stable (sensitivity variation within 2.5%) after 200 cycles of bending to radii of 25 mm, 40 mm, and 50 mm and 200 cycles of twisting to an angle of 120°.

(d) As predicted by theory (eq 1), the Seebeck coefficient for the printed sensors was dependent only upon the temperature difference and not upon the sensor dimensions (Figures 2 and 3) or manufacturing conditions. This result indicated manufacturability of nanoparticle-based sensors for device applications. The stable performance of the sensor after the mechanical cycles was attributed to the porous geometry of the films, where the additional free surfaces due to porosity enable large strains without a proportional build-up of the internal stresses.

(e) A manufacturing framework is created for a new class of nanoparticle-based devices on flexible substrates with a linear and stable performance for various existing and emerging applications.

■ ASSOCIATED CONTENT

Supporting Information

The Supporting Information is available free of charge on the ACS Publications website at DOI: 10.1021/acsanm.9b00628.

TEM sample preparation, SEM images, porosity, XP spectra, 3D scan of sensor segment, wrinkle height data, and optical images of films (PDF)

■ AUTHOR INFORMATION

Corresponding Author

*E-mail: rpanat@andrew.cmu.edu.

ORCID

Andrew Gellman: 0000-0001-6618-7427

Rahul Panat: 0000-0002-4824-2936

Present Address

⊥M.T.R.: Intel Corporation, 5000 W. Chandler Boulevard, Chandler, AZ 85226, U.S.

Notes

The authors declare no competing financial interest.

■ ACKNOWLEDGMENTS

This work was partly supported by the U.S. Department of Energy, National Energy Technology Laboratory (NETL), under Grant DE-FE0026170. The microscopy work was performed at the Nanoscience Fabrication and Characterization facility at the University of Pittsburgh under CMU-Pittsburgh collaborative agreement.

■ REFERENCES

(1) Rajagopal, M. C.; Valavala, K. V.; Gelda, D.; Ma, J.; Sinha, S. Fabrication and Characterization of Thermocouple Probe for Use in Intracellular Thermometry. *Sens. Actuators, A* **2018**, *272*, 253.

(2) Yang, F.; Li, G.; Yang, J.; Wang, Z.; Han, D.; Zheng, F.; Xu, S. Measurement of local temperature increments induced by cultured HepG2 cells with micro-thermocouples in a thermally stabilized system. *Sci. Rep.* **2017**, *7* (1), 1721.

(3) Murakami, R.; Kamada, K.; Shoji, Y.; Yokota, Y.; Yoshino, M.; Kurosawa, S.; Ohashi, Y.; Yamaji, A.; Yoshikawa, A. Fabrication of Flexible Ir and Ir-Rh Wires and Application for Thermocouple. *J. Cryst. Growth* **2018**, *487*, 72−77.

DOI: 10.1021/acsanm.9b00628
ACS Appl. Nano Mater. 2019, 2, 3280−3291

Downloaded via CARNEGIE MELLON UNIV on March 08, 2025 at 06:46:59 (UTC). See https://pubs.acs.org/sharingguidelines for options on how to legitimately share published articles.

(4) Oh, J. H.; Hong, S. Y.; Park, H.; Jin, S. W.; Jeong, Y. R.; Oh, S. Y.; Yun, J.; Lee, H.; Kim, J. W.; Ha, J. S. Fabrication of High-Sensitivity Skin-Attachable Temperature Sensors with Bioinspired Microstructured Adhesive. *ACS Appl. Mater. Interfaces* **2018**, *10* (8), 7263−7270.
(5) Xie, Y.; Xie, R.; Yang, H.-C.; Chen, Z.; Hou, J.; López-Barrón, C. R.; Wagner, N. J.; Gao, K.-Z. Iono-Elastomer-Based Wearable Strain Sensor with Real-Time Thermomechanical Dual Response. *ACS Appl. Mater. Interfaces* **2018**, *10* (38), 32435−32443.
(6) Gregory, O. J.; Busch, E.; Fralick, G. C.; Chen, X. Preparation and characterization of ceramic thin film thermocouples. *Thin Solid Films* **2010**, *518* (21), 6093−6098.
(7) Snyder, G. J. Thermoelectric Energy Harvesting. In *Energy Harvesting Technologies*; Priya, S., Inman, D. J., Eds.; Springer US: Boston, MA, 2009; pp 325−336.
(8) Zhang, B.; Sun, J.; Katz, H.; Fang, F.; Opila, R. Promising thermoelectric properties of commercial PEDOT: PSS materials and their Bi2Te3 powder composites. *ACS Appl. Mater. Interfaces* **2010**, *2* (11), 3170−3178.
(9) Zhao, X.; Li, H.; Yang, K.; Jiang, S.; Jiang, H.; Zhang, W. Annealing effects in ITO based ceramic thin film thermocouples. *J. Alloys Compd.* **2017**, *698*, 147−151.
(10) Marr, M. A.; Wallace, J. S.; Chandra, S.; Pershin, L.; Mostaghimi, J. A fast response thermocouple for internal combustion engine surface temperature measurements. *Exp. Therm. Fluid Sci.* **2010**, *34* (2), 183−189.
(11) Freund, L. B.; Suresh, S. *Thin Film Materials: Stress, Defect Formation and Surface Evolution*; Cambridge University Press, 2004.
(12) Cho, J. H.; Lee, J.; Xia, Y.; Kim, B.; He, Y.; Renn, M. J.; Lodge, T. P.; Frisbie, C. D. Printable ion-gel gate dielectrics for low-voltage polymer thin-film transistors on plastic. *Nat. Mater.* **2008**, *7* (11), 900.
(13) Yang, C.; Zhou, E.; Miyanishi, S.; Hashimoto, K.; Tajima, K. Preparation of active layers in polymer solar cells by aerosol jet printing. *ACS Appl. Mater. Interfaces* **2011**, *3* (10), 4053−4058.
(14) Xie, W.; Zhang, X.; Leighton, C.; Frisbie, C. D. 2D Insulator−Metal Transition in Aerosol Jet Printed Electrolyte Gated Indium Oxide Thin Film Transistors. *Adv. Electr. Mater.* **2017**, *3* (3), 1600369.
(15) Thompson, B.; Yoon, H.-S. Aerosol-printed strain sensor using PEDOT: PSS. *IEEE Sens. J.* **2013**, *13* (11), 4256−4263.
(16) Draper, G. L.; Dharmadasa, R.; Staats, M. E.; Lavery, B. W.; Druffel, T. Fabrication of elemental copper by intense pulsed light processing of a copper nitrate hydroxide ink. *ACS Appl. Mater. Interfaces* **2015**, *7* (30), 16478−16485.
(17) Parhami, F.; McMeeking, R.; Cocks, A.; Suo, Z. A model for the sintering and coarsening of rows of spherical particles. *Mech. Mater.* **1999**, *31* (1), 43−61.
(18) Danaei, R.; Varghese, T.; Ahmadzadeh, M.; McCloy, J.; Hollar, C.; Sadeq Saleh, M.; Park, J.; Zhang, Y.; Panat, R. Ultrafast Fabrication of Thermoelectric Films by Pulsed Light Sintering of Colloidal Nanoparticles on Flexible and Rigid Substrates. *Adv. Eng. Mater.* **2019**, *21* (1), 1800800.
(19) Rahman, M. T.; Rahimi, A.; Gupta, S.; Panat, R. Microscale additive manufacturing and modeling of interdigitated capacitive touch sensors. *Sens. Actuators, A* **2016**, *248*, 94−103.
(20) Yang, H.; Rahman, M. T.; Du, D.; Panat, R.; Lin, Y. 3-D printed adjustable microelectrode arrays for electrochemical sensing and biosensing. *Sens. Actuators, B* **2016**, *230*, 600−606.
(21) Rahman, M. T.; Moser, R.; Zbib, H. M.; Ramana, C.; Panat, R. 3-D printed high performance strain sensors for high temperature applications. *J. Appl. Phys.* **2018**, *123* (2), 024501.
(22) Ha, M.; Seo, J.-W. T.; Prabhumirashi, P. L.; Zhang, W.; Geier, M. L.; Renn, M. J.; Kim, C. H.; Hersam, M. C.; Frisbie, C. D. Aerosol Jet Printed, Low Voltage, Electrolyte Gated Carbon Nanotube Ring Oscillators with Sub-5 μs Stage Delays. *Nano Lett.* **2013**, *13* (3), 954−960.
(23) Mette, A.; Richter, P.; Hörteis, M.; Glunz, S. Metal aerosol jet printing for solar cell metallization. *Prog. Photovoltaics* **2007**, *15* (7), 621−627.
(24) Goth, C.; Putzo, S.; Franke, J. In Aerosol jet printing on rapid prototyping materials for fine pitch electronic applications. 2011 IEEE 61st Electronic Components and Technology Conference (ECTC); IEEE, 2011; pp 1211−1216.
(25) Panat, R. P.; Heo, D. H. Three-dimensional passive components. U.S. Patent 9969001, May 2018.
(26) Rahman, M. T.; Renaud, L.; Renn, M.; Heo, D.; Panat, R. Aerosol Based Direct-Write Micro-Additive Fabrication Method for Sub-mm 3-D Metal-Dielectric Structures. *J. Micromech. Microeng.* **2015**, *25* (10), 107002.
(27) Rahman, M. T.; McCloy, J.; Ramana, C. V.; Panat, R. Structure, electrical characteristics, and high-temperature stability of aerosol jet printed silver nanoparticle films. *J. Appl. Phys.* **2016**, *120* (7), 075305.
(28) Mahajan, A.; Frisbie, C. D.; Francis, L. F. Optimization of aerosol jet printing for high-resolution, high-aspect ratio silver lines. *ACS Appl. Mater. Interfaces* **2013**, *5* (11), 4856−4864.
(29) Perelaer, J.; Klokkenburg, M.; Hendriks, C. E.; Schubert, U. S. Microwave flash sintering of inkjet printed silver tracks on polymer substrates. *Adv. Mater.* **2009**, *21* (47), 4830−4834.
(30) MacNeill, W.; Choi, C.-H.; Chang, C.-H.; Malhotra, R. On the self-damping nature of densification in photonic sintering of nanoparticles. *Sci. Rep.* **2015**, *5*, 14845.
(31) Araki, T.; Sugahara, T.; Jiu, J.; Nagao, S.; Nogi, M.; Koga, H.; Uchida, H.; Shinozaki, K.; Suganuma, K. Cu salt ink formulation for printed electronics using photonic sintering. *Langmuir* **2013**, *29* (35), 11192−11197.
(32) Danaei, R.; Varghese, T.; Ahmadzadeh, M.; McCloy, J.; Hollar, C.; Sadeq Saleh, M.; Park, J.; Zhang, Y.; Panat, R. Ultrafast Fabrication of Thermoelectric Films by Pulsed Light Sintering of Colloidal Nanoparticles on Flexible and Rigid Substrates. *Adv. Eng. Mater.* **2019**, *21*, 1800800.
(33) Crandall, S. H.; Dahl, N. C.; Lardner, T. J.; Sivakumar, M. *An Introduction to Mechanics of Solids*; Tata McGraw-Hill Education, 2012.
(34) Lu, N.; Kim, D.-H. Flexible and stretchable electronics paving the way for soft robotics. *So. Robot.* **2014**, *1* (1), 53−62.
(35) Vuorinen, T.; Laurila, M.-M.; Mangayil, R.; Karp, M.; Mäntysalo, M. In High Resolution E-Jet Printed Temperature Sensor on Artificial Skin. European Medical and Biological Engineering Conference, Singapore; Springer Singapore, Singapore, 2018; pp 839−842.
(36) Suarez, F.; Parekh, D. P.; Ladd, C.; Vashaee, D.; Dickey, M. D.; Öztürk, M. C. Flexible thermoelectric generator using bulk legs and liquid metal interconnects for wearable electronics. *Appl. Energy* **2017**, *202*, 736−745.
(37) Rim, Y. S.; Bae, S. H.; Chen, H.; De Marco, N.; Yang, Y. Recent progress in materials and devices toward printable and flexible sensors. *Adv. Mater.* **2016**, *28* (22), 4415−4440.
(38) Wilson, W. C.; Atkinson, G. M. Passive wireless sensor applications for NASA's extreme aeronautical environments. *IEEE Sens. J.* **2014**, *14* (11), 3745−3753.
(39) Watson, J.; Castro, G. A review of high-temperature electronics technology and applications. *J. Mater. Sci.: Mater. Electron.* **2015**, *26* (12), 9226−9235.
(40) Renn, M. J.; Essien, M.; King, B. H.; Paulsen, J. A. Aerodynamic jetting of aerosolized fluids for fabrication of passive structures. U.S. Patent 7674671 B2, 2010.
(41) Renn, M. J.; Schrandt, M.; Renn, J.; Feng, J. Q. Localized Laser Sintering of Metal Nanoparticle Inks Printed with Aerosol Jet® Technology for Flexible Electronics. *J. Microelectron. Electron. Packag.* **2017**, *14* (4), 132−139.
(42) Paul, B. K.; Panat, R.; Mastrangelo, C.; Kim, D.; Johnson, D. Manufacturing of Smart Goods: Current State, Future Potential, and Research Recommendations. *J. Micr. Nan. Manuf.* **2016**, *4* (4), 044001.
(43) Saleh, M. S.; Hu, C.; Panat, R. Three-dimensional micro-architected materials and devices using nanoparticle assembly by pointwise spatial printing. *Sci. Adv.* **2017**, *3* (3), No. e1601986.

DOI: 10.1021/acsanm.9b00628
ACS Appl. Nano Mater. 2019, 2, 3280−3291

Downloaded via CARNEGIE MELLON UNIV on March 08, 2025 at 06:46:59 (UTC). See https://pubs.acs.org/sharingguidelines for options on how to legitimately share published articles.

(44) Saleh, M. S.; HamidVishkasougheh, M.; Zbib, H.; Panat, R. Polycrystalline micropillars by a novel 3-D printing method and their behavior under compressive loads. *Scr. Mater.* **2018**, *149*, 144−149.
(45) Ryu, J.; Kim, H.-S.; Hahn, H. T. Reactive sintering of copper nanoparticles using intense pulsed light for printed electronics. *J. Electron. Mater.* **2011**, *40* (1), 42−50.
(46) Pál, E.; Kun, R.; Schulze, C.; Zöllmer, V.; Lehmhus, D.; Bäumer, M.; Busse, M. Composition-dependent sintering behaviour of chemically synthesised CuNi nanoparticles and their application in aerosol printing for preparation of conductive microstructures. *Colloid Polym. Sci.* **2012**, *290* (10), 941−952.
(47) Volkert, C. A.; Minor, A. M. Focused ion beam microscopy and micromachining. *MRS Bull.* **2007**, *32* (5), 389−399.
(48) Ishitani, T.; Kaga, H. Calculation of local temperature rise in focused-ion-beam sample preparation. *Microscopy* **1995**, *44* (5), 331−336.
(49) Suvorova, E.; Buffat, P. Electron diffraction from micro-and nanoparticles of hydroxyapatite. *J. Microsc.* **1999**, *196*, 46−58.
(50) Biesinger, M. C.; Lau, L. W. M.; Gerson, A. R.; Smart, R. S. C. Resolving surface chemical states in XPS analysis of first row transition metals, oxides and hydroxides: Sc, Ti, V, Cu and Zn. *Appl. Surf. Sci.* **2010**, *257* (3), 887−898.
(51) Brongersma, H. H.; Sparnaay, M. J.; Buck, T. M. Surface segregation in Cu-Ni and Cu-Pt alloys; A comparison of low-energy ion-scattering results with theory. *Surf. Sci.* **1978**, *71* (3), 657−678.
(52) Kuijers, F. J.; Ponec, V. The surface composition of the nickel-copper alloy system as determined by Auger electron spectroscopy. *Surf. Sci.* **1977**, *68*, 294−304.
(53) King, T. S.; Donnelly, R. G. Recent developments in modeling binary alloy surface segregation: Low index planes, steps, kinks, and chemisorption. *Surf. Sci.* **1984**, *141* (2), 417−454.
(54) Webber, P. R.; Rojas, C. E.; Dobson, P. J.; Chadwick, D. A combined XPS/AES study of Cu segregation to the high and low index surfaces of a Cu-Ni alloy. *Surf. Sci.* **1981**, *105* (1), 20−40.
(55) Foiles, S. M. Calculation of the surface segregation of Ni-Cu alloys with the use of the embedded-atom method. *Phys. Rev. B: Condens. Matter Mater. Phys.* **1985**, *32* (12), 7685−7693.
(56) Ruban, A. V.; Skriver, H. L.; Nørskov, J. K. Surface segregation energies in transition-metal alloys. *Phys. Rev. B: Condens. Matter Mater. Phys.* **1999**, *59* (24), 15990−16000.
(57) Manoylov, A.; Borodich, F. M.; Evans, H. P. Modelling of elastic properties of sintered porous materials. *Proc. R. Soc. London, Ser. A* **2013**, *469* (2154), 20120689.
(58) Dou, R.; Xu, B.; Derby, B. High-strength nanoporous silver produced by inkjet printing. *Scr. Mater.* **2010**, *63* (3), 308−311.
(59) Papka, S. D.; Kyriakides, S. In-plane compressive response and crushing of honeycomb. *J. Mech. Phys. Solids* **1994**, *42* (10), 1499−1532.
(60) Chen, Y.; Li, T.; Jia, Z.; Scarpa, F.; Yao, C.-W.; Wang, L. 3D printed hierarchical honeycombs with shape integrity under large compressive deformations. *Mater. Des.* **2018**, *137*, 226−234.
(61) Minev, I. R.; Musienko, P.; Hirsch, A.; Barraud, Q.; Wenger, N.; Moraud, E. M.; Gandar, J.; Capogrosso, M.; Milekovic, T.; Asboth, L.; Torres, R. F.; Vachicouras, N.; Liu, Q.; Pavlova, N.; Duis, S.; Larmagnac, A.; Vörös, J.; Micera, S.; Suo, Z.; Courtine, G.; Lacour, S. P. Electronic dura mater for long-term multimodal neural interfaces. *Science* **2015**, *347* (6218), 159−163.
(62) Tekin, E.; de Gans, B.-J.; Schubert, U. S. Ink-jet printing of polymers−from single dots to thin film libraries. *J. Mater. Chem.* **2004**, *14* (17), 2627−2632.

DOI: 10.1021/acsanm.9b00628
ACS Appl. Nano Mater. 2019, 2, 3280−3291